Ion Formation from Rapidly Heated Aqueous Droplets by Droplet Assisted Ionization

Michael J. Apsokardu; Justin M. Krasnomowitz; Shuai Jiang; Murray V. Johnston*

Department of Chemistry and Biochemistry, University of Delaware, Newark, DE, 19716

Abstract

When aqueous droplets travel through a temperature-controlled capillary from atmospheric pressure into a vacuum, they undergo aerodynamic and/or thermal breakup to give charged progeny droplets that subsequently produce gas-phase molecular ions from solutes that were in the original droplets. This phenomenon is the basis of droplet assisted ionization (DAI), a method that was recently developed for online characterization of aerosols by mass spectrometry. The conditions allowing initial droplets to break up into progeny droplets were studied by computational fluid dynamics (CFD) with a droplet evaporation model. The CFD results were then used to interpret experimental measurements of ion current vs. capillary wall temperature. For capillary wall temperatures below about 150 °C, the abilities of droplets to undergo either aerodynamic or thermal breakup are strongly temperature dependent. Above this temperature, the mode of initial droplet breakup becomes temperature independent, and the temperature dependence of the ion signal intensity can be explained in relation to ion formation from charged

progeny droplets. Activation energies for ion formation fall into two main categories: ~41 kJ mol⁻¹ for droplets containing predominantly nonionic solutes, which matches the enthalpy of vaporization for water and suggests a charge residue process for ion formation, and ~24 kJ mol⁻¹ for droplets containing salts, which suggests an ion evaporation process where the ion is ejected from the droplet surface within a cluster of solvent molecules.

Introduction

The ability to effectively analyze solutes in a liquid droplet by mass spectrometry is dependent on the ability to separate solute molecules from the solvent to produce gas-phase molecular ions. The two main mechanisms proposed for producing molecular ions from charged liquid droplets produced by electrospray ionization (ESI) are the ion evaporation (IEM)¹ and the charge residue models (CRM).² For IEM, molecular ions evaporate from the surface of the droplet, usually within in a cluster containing several solvent molecules. In the case of CRM, solvent evaporates completely, leaving just the molecular ion as the nonvolatile residue from the droplet. While IEM is typically thought to be more applicable to small molecular weight species and CRM for higher molecular weight species, the conditions needed to form gas-phase ions by each mechanism are still a matter of debate.³

Molecular dynamics (MD) simulations have become an effective tool to provide perspective into the relative roles of ions and solvent in the ion evaporation process, specifically in the final stages of droplet lifetime where the formation of gas-phase ions is thought to occur.⁴ For instance, MD simulations have provided visual interpretation to the transition state small ions enter prior to their eventual ejection from the droplet environment.⁵ Such studies allow researchers to distinguish ion formation by either IEM or CRM or even identify instances in which both

mechanisms are operative. Significant movement has been made recently towards the use of MD simulations to show how large chain polymers or proteins are ejected from droplets by a separate mechanism known as the chain ejection model (CEM). 7-9

The efficiency with which ions are formed is initially governed by the ability to induce droplet breakup and produce progeny droplets carrying a net charge. For ESI, charged droplets are produced by applying a high voltage to a liquid sample. As droplets evaporate in route to the inlet of the mass spectrometer, the charge density on the surface of the droplet increases until the Rayleigh limit is reached and Coulombic fission occurs, producing numerous smaller progeny droplets that also carry a net charge. 10 The source of charged progeny droplets is not so clear when the droplets entering the inlet of the mass spectrometer are initially uncharged, as is the case for a method such as droplet assisted ionization (DAI). DAI is method for producing ions from solutes in micron-size droplets by passing the droplets through a temperature-controlled capillary interface into the mass spectrometer.¹¹ Aerodynamic and thermal stressors inside the capillary are thought to induce droplet breakup, but they have not been studied in detail. Optimum conditions for producing ions by DAI have been investigated in previous work, ¹² and an important parameter is the wall temperature of the capillary, which can be precisely controlled from 25 to 850 °C. DAI shares many similarities to other inlet ionization techniques such as matrix assisted ionization (MAI) and solvent assisted ionization (SAI).^{13–15}

In DAI, the ion yield, defined as the fraction of solute molecules entering the inlet that are eventually detected as ions in the mass spectrum, exhibits a complex temperature dependence. Ion yield incorporates ionization efficiency, ion transmission efficiency and detector efficiency into a single parameter. As the capillary wall temperature increases from about 150 to 500 °C, the ion yield for most analytes increases monotonically by one to two orders of magnitude. Departures

from the monotonic increase are found with capillary temperatures outside this range. At the low end, the ion yield is often higher at 25 °C than in the 100-150°C range. At 25 °C, it has been proposed that droplets are subject to evaporative cooling inside the capillary as well as cooling in the gas expansion coming out of the capillary into the vacuum, which causes the droplets to freeze and shatter in a manner that produces a relatively large number of ions. Slightly higher temperatures produce lower ion yields, presumably because droplets are unable to freeze. At the high temperature end, the ion yield is analyte dependent but generally increases only slightly, if at all, above 500 °C. 11,12

The mechanism of ion formation by DAI can be thought of as a two-step process: breakup of the initial droplet to give charged progeny droplets, followed by gas-phase ion formation. These steps are illustrated in Figure 1. Since DAI mass spectra are remarkably similar to those obtained with ESI including formation of multiply charged ions, 11,12,18-21 the second step is thought to be the same for the two methods, where charged progeny droplets undergo successive iterations of evaporation and Coulombic fission until they become small enough for ion emission, which is thought to occur from droplets in the nanometer size range.⁴

In this work, computational fluid dynamics modeling (CFD) is combined with a numerical droplet evaporation model in order to identify conditions that allow aerodynamic and/or thermal breakup of an initially uncharged droplet inside the DAI capillary. Modeling results are discussed in the context of temperature-dependent ion signal intensities obtained experimentally. For capillary wall temperatures below about 150 °C, the abilities of droplets to undergo aerodynamic and thermal breakup are strongly temperature dependent, making the temperature dependence of the ion signal intensity difficult to interpret. Above this temperature, the mode of initial droplet breakup becomes temperature independent, and the temperature dependence of the ion signal

intensity gives insight specifically into the second step – gas phase ion formation from charged progeny droplets.

Experimental Methods

Computational Fluid Dynamics (CFD). The DAI capillary inlet was recreated in COMSOL Multiphysics 5.4 (Stockholm, Sweden, http://www.comsol.com) to perform computational fluid dynamics (CFD) calculations to characterize heat transfer from the wall into the air flow through the capillary. The capillary inlet geometry was recreated in COMSOL as a 2-D axi-symmetric model, and COMSOL's finite element method was used to solve for flows throughout. The geometry was automatically meshed with a physics-controlled sequence using normal sized free triangular and quad mesh elements. The final mesh consisted of 4837 elements with an average quality of 0.78. The element quality is a measure of cell distortion with a value of 1 indicating perfect element shape. A 2-D axi-symmetric model was chosen as a way to reconstruct and model the capillary inlet three dimensionally while reducing the computation cost and time. Finer mesh densities were tested but were too computationally intensive.

Once meshed, a turbulent, high Mach number flow (Spalart-Allmaras) model was used. In this model, the gas is treated as compressible for characterizing air flow through the capillary. The Reynold's number at the capillary inlet is ~2800. A conical geometry was placed at the exit of the capillary to simulate the first vacuum stage of the mass spectrometer. This region is taken to have a pressure of 100 Pa, which is measured and provided by the commercial mass spectrometer. Similar work has utilized parabolic geometries to simulate the vacuum region, but this was found to have no effect on the physics inside the capillary.²² The Particle Tracing Module within COMSOL was coupled to the CFD model to calculate the distribution of particle residence times

in the flow tube. CFD calculations were performed for a simulated time of 20 ms to allow steadystate conditions inside the capillary to be reached, at which point, particle tracing was performed. Particle tracing is performed for a simulated time of 2 ms with a 1 μ s time step. For these calculations, liquid droplets of 103 different diameters between the sizes 0.5 and 20 μ m were considered. Each droplet size was systematically studied one at a time. For each diameter, 9 liquid droplets with uniform radial starting positions were released at the opening of the DAI capillary inlet. The radial and axial positions of each droplet were traced, and the pressure, temperature, density, and dynamic viscosity of air were calculated along the paths. As an example, Figure S1 depicts the 9 radial starting positions and subsequent tracks through the capillary for a 5.2 μ m dia. droplet. Along track #9, Figure S2 shows the air pressure and corresponding water boiling point, while Figure S3 shows air velocity.

Droplet Evaporation Model. Computation of pressure and temperature dependent properties of evaporating water were based on the International Association for the Properties of Water and Steam using the Industrial Formulation 1997 (IAPWS-IF97).²³ The solution of the CFD calculations was directly interfaced with Steam97 Excel Add-In (MegaWatSoft Inc., Toronto, ON, Canada). The equations used in this formulation are valid between temperatures of 0 and 800 °C. and for pressures less than 100 MPa, thereby satisfying the needs of this work. This package allowed water density, dynamic viscosity, thermal diffusivity, and surface tension to be calculated as a function of both pressure and temperature.²³ These values are used as part of the droplet evaporation model to evaluate evaporation and breakup of droplets upon entering the DAI capillary interface.

The rate of evaporation $(\delta d_d/\delta t)$ of a liquid water droplet^{24,25} with diameter d_d is given by

$$(1) \frac{\partial d_d}{\partial t} = \frac{2D_w m_w}{\rho_d k_B T d_d} (\Delta P) \beta Sh$$

where D_w is the gas-phase diffusion coefficient of water, m_w is the mass of one water molecule, ρ_d is the density of the droplet, k_B is the Boltzmann constant, T is the temperature, d_d is the diameter of the droplet, ΔP is the pressure difference, β is the mass flux correction factor, and Sh is the Sherwood number. Equation 1 is specifically used to calculate the evaporation of a static droplet and is then corrected by Sh to account for changes in convection mass transfer in the surrounding air flow^{26–28}

(2) Sh =
$$(2 + 0.6Re_d^{1/2}Sc^{1/3})$$
.

In Equation 2, Re_d and Sc are the Reynold's and Schmidt numbers respectively. Complete definitions of all variables in Equations 1 and 2, plus additional discussion of the modeling procedure and results, are provided in the supporting information.

At the same time the change is droplet diameter by evaporation is calculated, the Weber number (We) of the droplet is also calculated and is given by 18

(3)
$$We = \frac{(v_{air} - v_d)^2 \rho_d d_d}{\sigma}$$

where v_{air} and v_{d} are the velocity of air and droplet respectively and σ is the surface tension of water. When We > 10, the droplet is considered able to breakup due to aerodynamic forces. $^{18,29-31}$ The droplet evaporation model is interfaced with the particle tracing module from CFD simulations by calculating the change in droplet diameter with a 1 μ s time step.

Aerosol Generation. A fine mist of micron-size droplets was produced with an atomizer (Model ATM226, TOPAS, Dresden, Germany) that were then sent directly into the mass spectrometer for analysis. The nonionic solutes studied were cortisone, sucrose, and polypropylene glycol (M_n 425 Da). In some experiments, salts including ammonium sulfate, sodium sulfate, and cesium iodide, were mixed with the nonionic solutes. Cesium iodide and tetrabutylammonium chloride salts were sampled alone. Solutes were purchased from Sigma Aldrich (St. Louis, MO).

Solutions were prepared with Optima grade water obtained from Fisher Scientific (Hampton, NH). Atomization was performed with 1 Lpm of house air from a Zero Air Generator 737 Series (Aadco Instruments, Cleveland, OH), which removed gas-phase ammonia and organics. Airflow into the atomizer was controlled with a mass flow controller (Dakota Instruments, Orangeburg, NY). Aerosol droplets containing polypropylene glycol (PPG) were generated from a 10 μ M solution. All other aerosols were generated from 100 μ M solutions of the respective solute. In experiments where nonionic solutes were mixed with salt compounds, the salt concentration was also 100 μ M. The droplet size distribution from the atomizer was reconstructed from the measured dry particle size distribution obtained from the 100 μ M cortisone solution.¹² The droplet distribution ranged from about 0.5 to 20 μ m with a median diameter of 2 μ m. 103 different droplet diameters were measured in this range. Although droplets at the high end of the distribution probably had very low transmission efficiencies through the experimental apparatus, this effect does not change the conclusions of the study since the temperature dependence of droplet breakup is greatest for droplets in the lower end of the size distribution.

Mass Spectrometry. Mass analysis was performed with a Waters SYNAPT G2-S quadrupole ion mobility time-of-flight mass spectrometer, which was outfitted with a customized atmospheric pressure inlet consisting of a stainless-steel capillary tube (69 mm length, 1 mm o.d., 0.5 mm i.d.). The first 20 mm of the capillary was unheated, while the remaining portion of capillary could be heated up to 289 °C by applying a voltage to 24-gauge NiChrome wire that was encased in a ceramic insulating jacket around the capillary. The capillary wall temperature was measured with a thermocouple probe and precisely controlled with a homemade temperature control box containing a solid-state relay (Omega, Stamford, CT) and variable power supply. Previous work for DAI utilized a wall temperature as high as 850 °C. 11,12 The ceramic cartridge

heater was redesigned for the current project to evenly heat the capillary from all sides and is the reason for the slightly different capillary wall temperature range in this study relative to the past. Aerosol droplets entered through one port of a ¼ inch Swage-lok fitting. The (unheated) entrance end of the capillary extended into a one-sixteenth inch fitting and was sealed with a Teflon ferrule. Other settings of the mass spectrometer were: source temperature 100 °C, cone voltage 10 V, and offset voltage 60 V. Changing these settings over a substantial range of values did not affect relative ion signals. Droplets entered the capillary at atmospheric pressure and exited into the first vacuum stage of the mass spectrometer where the base pressure is 100 Pa.

Results and Discussion

Conditions allowing thermal and/or aerodynamic breakup of aqueous, uncharged droplets (Step 1 in Figure 1) were identified using CFD in combination with a droplet evaporation model. These conditions were found to be strongly temperature dependent and are illustrated in Figures 2 and 3 for the example of a $5.2 \,\mu \mathrm{m}$ dia. droplet following the track closest to the capillary wall (#9 in Figure S1). The conditions are then extended to droplets of other sizes and flow tracks through the capillary, and finally compared to experimentally measured changes in ion signal intensity with temperature.

Thermal Breakup of Droplets. Figure 2 shows how a $5.2 \,\mu$ m diameter droplet evaporates as it moves through the capillary for wall temperatures of a) 25, b) 100, and c) 289 °C. In these plots, the capillary entrance is 0 mm, the exit is 69 mm, and the point at which heating (if any) begins is 20 mm. The droplet diameter and temperature are plotted as a function of distance through the capillary, and the boiling point of water (changes with changing pressure inside the capillary) is shown for reference. The temperatures of the air and droplet are assumed to be the

same. The validity of this assumption is explained below. When the capillary wall is maintained at 25 °C (Figure 2a), evaporation causes the droplet diameter to decrease only by ~0.3%. The temperature slowly decreases, and at ~55 mm the droplet freezes, and no further evaporation occurs. Previous work has speculated that droplets freeze inside an unheated capillary and shatter in a way that is able to form ions. Figure 2a confirms that freezing can indeed occur.

When the capillary wall is heated to $100\,^{\circ}\text{C}$ (Figure 2b), droplet evaporation is still minimal (~1% reduction in diameter) because the temperature does not get close to the boiling point. When the capillary wall is heated to 289 °C K (Figure 2c), the droplet initially evaporates slowly and when the temperature reaches the boiling point at ~35 mm, the droplet flash evaporates over a time period smaller than the 1 μ s time step used in the simulations. Between the point where heating of the capillary begins (20 mm) and when the boiling point is reached, the droplet heating rate is $7\times10^5\,\text{K}\,\text{s}^{-1}$ (Figure S4). By comparison, a droplet of this size would thermally equilibrate over the same temperature as Figure S4 at a faster rate, $9\times10^5\,\text{K}\,\text{s}^{-1}$, confirming that the droplet temperature can reasonably track the surrounding air temperature up to and including the flash evaporation event.

The flash evaporation event in Figure 2c is considered to be a marker for thermal breakup of the droplet. It has been known for many years that rapidly heated droplets having a surface charge well below the Rayleigh limit can burst, producing hundreds of progeny droplets.³² The droplet heating rate inside the capillary is similar to the heating rate in MALDI, which is estimated to be on the order $10^6 - 10^{12}$ K s⁻¹, suggesting that the underlying concept of rapid heating and explosive vaporization of the condensed phase is also similar.^{33–35}

Figure 2c illustrates thermal breakup for one combination of air track through the capillary and wall temperature. For other combinations, thermal breakup occurs when the temperature

reaches the boiling point of water, which can vary several mm from the location in Figure 2c. (See Figure S5 for an example.) The boiling point, and hence the temperature when thermal breakup occurs, may also change by ~2 degrees since the pressure changes slightly with distance in this region of the capillary (Figure S2). However, this effect is a small perturbation of the overall process.

Aerodynamic Breakup of Droplets. An aerodynamic force is exerted on droplets inside the capillary since the velocity of the gas surrounding the droplet is different from the droplet velocity. The Weber number (We) described by Eq. 3, is a dimensionless number used to assess whether or not the aerodynamic force is sufficient for droplet breakup. In general, if We > 10, the droplet is considered able to breakup. For We < 10, the aerodynamic force does not exceed the force of surface tension, and the droplet cannot breakup. 18,29,30

Figure 3 shows We vs. distance inside the capillary for the 5.2 μ m dia. droplet in Figure 2 and two different capillary temperatures, 100 and 289 °C, for cases in which flash evaporation does not and does occur respectively. When the capillary is heated to 100 °C, We exceeds 10 before the droplet that has traveled 10 mm into the capillary. If the droplet does not breakup at this point, We continues to increase as the droplet moves through the capillary and exceeds 10^3 at the exit. While the droplet does not undergo thermal breakup, it is highly likely that aerodynamic breakup occurs somewhere along the capillary. Also shown in Figure 3 is We vs. distance when the capillary wall is heated to 289 °C. We reaches a value of 10 between 10 and 15 mm into the capillary, but then increases to > 10^2 prior to flash evaporation point at ~35 mm. This droplet is also likely to undergo aerodynamic breakup, though thermal breakup will ultimately occur if the timescale for aerodynamic breakup is greater than about 115μ s.

Because the velocity difference between a droplet and the surrounding air increases with increasing droplet diameter, larger droplets experience a greater aerodynamic force than smaller droplets. This effect is illustrated in Figure S6 where We vs. distance inside the capillary is plotted for droplet diameters of 1.0, 2.0, and 5.2 μ m with a wall temperature of 100 °C. We for the 1.0 and 2.0 μ m dia. droplets do not exceed 10 until just before the capillary exit. While aerodynamic breakup near the capillary exit is possible for small droplets with a low wall temperature, they are more likely to undergo thermal breakup earlier in the capillary when the wall temperature is high enough to cause flash vaporization.

Temperature Dependence of Thermal and Aerodynamic Breakup. The illustrations in Figures 2 and 3 show how conditions for thermal and aerodynamic breakup can be identified and that the probability of each is strongly dependent on capillary wall temperature. This dependence is explored in Figures 4 and 5 for a droplet size distribution generated with a commercial atomizer. As described in the Experimental Methods section, the droplet size distribution for the DAI measurements in this study was inferred from dry particle size distribution generated by atomizing a 100 μM cortisone solution. Thermal and aerodynamic breakup were modeled for droplet diameters across the size distribution with the capillary wall temperatures that were studied experimentally. For each wall temperature, a total of 927 droplets were evaluated: 103 different diameters with 9 droplet radial starting positions (Figure S1) for each diameter. Six wall temperatures were examined, and the results from four of these are shown in Figure 4.

For the lowest two wall temperatures, 25 and 100 °C in Figures 4a and b respectively, the air temperature never reaches the boiling point, so thermal breakup does not occur. For a wall temperature of 25 °C (Figure 4a), droplets at the lower end of the size range freeze before *We* exceeds 10 and can break up only if they shatter as discussed previously. Droplets at the higher

end of the size range are capable of aerodynamic breakup since *We* exceeds 10 prior to freezing. For a wall temperature of 100 °C (Figure 4b), freezing no longer occurs and most droplets are capable of aerodynamic breakup, with the exception of the smallest droplets below about 0.8 μm in diameter.

For a wall temperature of 150 °C (Figure 4c), some droplets are able to undergo thermal breakup. These droplets follow air traces closer to the wall, where the air temperature is higher than along the centerline of the capillary. The largest droplets in the size distribution follow the centerline more closely than smaller droplets and are unable to flash evaporate, but they are capable of aerodynamic breakup. For wall temperatures above 150 °C, as exemplified by the 289 °C plot in Figure 4d, all droplets are able to flash evaporate and therefore undergo thermal breakup, though droplets in the high end of the distribution could undergo aerodynamic breakup before thermal breakup occurs.

The plots in Figure 4 along with those from other capillary wall temperatures studied, are summarized in Figure 5a, where the percentage of droplets capable of aerodynamic and/or thermal breakup are plotted vs. wall temperature. In this plot, droplets that are considered capable of thermal breakup include those that reach We > 10 prior to thermal breakup, since the timescale of aerodynamic breakup is not known. For this reason, the percentages for higher wall temperatures add up to greater than 100%. Two important conclusions can be drawn from Figure 5a. First, for capillary wall temperatures above 100 C°, all droplets are capable of undergoing either aerodynamic or thermal breakup, and the percentage of droplets undergoing thermal breakup increases with increasing wall temperature. Second, for wall temperatures above than 150 C°, the mode of droplet breakup (aerodynamic vs. thermal) becomes independent of wall temperature and most droplets undergo thermal breakup.

Temperature Dependence of Ion Formation. The modeling results presented above have important implications for how experimental measurements of the temperature dependence of the DAI ion signal are interpreted. Referring back to Figure 1, ion formation in DAI involves two steps: 1) breakup of the initial uncharged droplet into smaller progeny droplets carrying a net charge and 2) ejection of ions from the progeny droplets into the gas phase. In principle, both steps can be temperature dependent. Fortunately, modeling gives insight into when the temperature dependence of the first step does or does not contribute substantially to the overall temperature dependence.

First, it is important to note that modeling does not predict charging of progeny droplets, just when they are or are not produced. We do know that charging is a rare occurrence since the ion yield (fraction of analyte molecules entering the capillary that are ultimately registered as ion counts at the detector) is at best 10⁻⁵ for our mass spectrometer. The extent to which charging depends on the mechanism of droplet breakup (freezing, aerodynamic, thermal) or the temperature at the point of breakup is unknown. Second, modeling shows that the mechanism of droplet breakup is not temperature dependent above a wall temperature of 150 °C (Figure 5a). Third, most droplets undergo thermal breakup when the wall temperature is above 150 °C. While the location within the capillary where thermal breakup occurs does vary with wall temperature and air track (Figure S5), the droplet temperature (boiling point of water) during breakup is essentially constant both droplet-to-droplet and as a function of wall temperature (Figure S2). Therefore, the temperature dependence of the ion signal for wall temperatures above 150 °C informs uniquely on the temperature dependence of Step 2, ion emission from the progeny droplets, which occurs downstream from and at a higher temperature than the thermal breakup event.

In Figure 5, the capillary wall temperature dependence of droplet breakup (Figure 5a) is compared to the temperature dependence of the DAI ion signal intensity experimentally measured for droplets atomized from a 100 µM cortisone solution (Figure 5b). Figure 5b shows that ion signal can be obtained at 25 °C without applying any heat to the capillary. Ion formation without heating is supported by the modeling results from Figures 4a and 5a, which show many droplets can undergo freezing or aerodynamic breakup (Step 1). When the capillary wall is heated slightly above this level, the relative contributions of different breakup mechanisms change, and it is not possible to separate temperature-dependent effects of Step 1 from Step 2. For capillary wall temperatures above 150 °C, Figure 5b shows that the ion signal intensity increases monotonically with increasing wall temperature, and this increase must be attributed to the temperature dependence of Step 2. The monotonic increase of the cortisone signal intensity in Figure 5b is also observed for droplets containing other nonionic solutes (sucrose, polypropylene glycol), salts (tetrabutylammonium chloride, cesium iodide), and mixtures of the two (cortisone mixed with ammonium sulfate, sodium sulfate, or cesium iodide).

The temperature dependence of the ion signal intensity can be used to estimate the activation energy (E_a) for ion formation. Since the signal intensity continues to increase with wall temperature above 150 °C, but the temperature at which droplets undergo thermal breakup in Step 1 remains constant, the continuing increase of the signal intensity indicates that ion emission from the progeny droplets (Step 2) occurs downstream from the location of droplet breakup where the air temperature is higher and scales with capillary wall temperature. (See Figure 2c.) For this reason, an Arrhenius plot is constructed where the temperature is taken as the maximum temperature (T_{max}) along the centerline of the gas flow. The calculation is performed in the following way:

(4)
$$\ln(I_{cps}) = \ln(A) - \left(\frac{E_a}{R}\right) \left(\frac{1}{T_{max}}\right)$$

where I_{cps} is the ion signal as counts per second, R is the universal gas constant, E_a is the activation energy, and T_{max} is the maximum air temperature along the centerline of the capillary for the wall temperature used in the measurement. In a traditional Arrhenius plot, the ordinate is given as R in R where R is the rate constant for ion formation. Unfortunately, the rate constant is not directly measured in this work. However, R_{cps} is directly proportional to R since the mass flow of analyte, R in R through the capillary is constant throughout any individual experiment:

(5)
$$I_{cps} = k [N]$$

The Arrhenius plot for droplets generated from the 100 μ M cortisone solution is shown in Figure 6, where the T_{max} values in this plot correspond to the capillary wall temperatures plotted in Figure 5b. The correlation between capillary wall temperature and T_{max} is shown in Figure S7. The plot in Figure 6 is linear and extends to lower temperatures than the top three temperatures in Figure 5b, indicating that even at somewhat lower temperatures, Step 2 is the main contributor to the temperature dependence. From this plot, E_a is determined to be 42 ± 1 kJ mol⁻¹. This value can be regarded as an upper limit since droplets following a trajectory closer to the capillary wall than the centerline will experience higher temperatures, and proportionally higher temperatures for each of the signal intensities would result in a lower calculated activation energy. If the capillary wall temperature is used in the Arrhenius calculation instead of T_{max} , E_a would be 36 kJ mol⁻¹, which represents a lower limit. While a different assumption for temperature in the Arrhenius plot will give a different absolute value of the activation energy, the relative differences discussed below among droplets containing different solutes is still valid.

Activation energies were also determined for DAI analysis two other nonionic solutes, polypropylene glycol (PPG) and sucrose, and these values are tabulated along with cortisone in Table 1. The activation energies for all three solutes are remarkably similar to each other. It is

important to note, for E_a to be properly defined, T_{max} must be occur at the same pressure for each capillary temperature. T_{max} was reached at essentially the same air pressure $(5.2 \pm 0.4 \times 10^4 \text{ Pa})$ for all capillary wall temperatures, making T_{max} suitable to use for determining E_a . The enthalpy of vaporization of water at this pressure is 42 kJ mol⁻¹ (41 kJ mol⁻¹ at 100 °C and $1.01 \times 10^5 \text{ Pa}$), ³⁶ is similar to E_a evaluated for all three nonionic solutes in Table 1. The similarities of the different solutes suggests that the ability to form ions from nonionic solutes is an intrinsic property of the solvent, in this case water, and that ion formation in Step 2 is associated with solvent vaporization, which would correspond to a charge residue mechanism.³⁷

While no salts were intentionally added to the solutions used to make these droplets, the observation of sodiated adducts in the mass spectra indicate that some salt contamination is present. To quantify the level of sodium contamination, flame atomic absorption was used to determine the sodium content of the bulk solutions used to create the droplets, giving a concentration of $1.0 \pm 0.8 \,\mu\text{M}$. While this concentration is quite low, Na⁺ is known to bind strongly with alcohol and carbonyl groups in the gas phase.^{38–40} This level of contamination provides useful reference for experiments where salts are intentionally added to the solutions.

The influence of salts on the temperature dependence of the cortisone signal intensity is shown in Figure 6 for droplets generated from a 100 μ M cortisone solution containing 100 μ M ammonium sulfate (blue) or sodium sulfate (green). The signal intensity increases more slowly with increasing temperature when the ionic solute is added, which results in a lower E_a as shown in Table 1: 27 \pm 1 and 24 \pm 1 kJ mol⁻¹ in the presence of an equimolar amount of ammonium and sodium sulfate respectively. Table 1 also shows activation energies for an additional experiment for 1:1 cortisone and cesium iodide and then for two experiments without cortisone, one for droplets containing just cesium iodide and the other for tetrabutylammonium chloride. As shown

in Table 1, the activation energies for ion formation from all droplets containing various salts are similar to each other and distinct from those containing nonionic solutes alone. The ion formation process is clearly different in the presence of salts, and the lower value of E_a suggests participation of an ion evaporation mechanism where solute ions are ejected from the surface of a progeny droplet within a cluster of solvent molecules. Although charge residue is likely to remain the dominant pathway for ion formation, ion evaporation plays a secondary role allowing progeny droplets to shed charge during droplet evaporation.^{6,37}

In the original work of Iribarne and Thomson, ion mobility was used to determine the evaporation rate of Na⁺ from droplets. From this work, the free energy of ion formation (ΔG^{\ddagger}) was determined, via transition state theory, to be 38 kJ mol⁻¹. The mechanism of gas-phase Na⁺ ion formation was ascribed to the ion evaporation model (IEM). Additional ion mobility spectrometry and modeling studies have since provided improvements to this original work by better predicting the effects of droplet polarization^{25,41} and radius of curvature on ion evaporation,^{25,42–44} while still finding good agreement with the original work. Ahadi et. al. also predicted ΔG^{\ddagger} for the evaporation of NH₄⁺ from water droplets by determining the rate constant for NH₄⁺ evaporation during molecular dynamics simulations.⁴⁵ They reported ΔG^{\ddagger} to be 32 kJ mol⁻¹ and went on to speculate that a similar ion evaporation mechanism would be operative for other small analytes such as protonated drugs or metabolites.

While the activation energies reported Table 1 are not directly comparable to the ΔG^{\ddagger} values reported previously, they do suggest that two distinct ion formation processes exist for Step 2 of DAI. One appears to be correlated with evaporation of solvent to dryness, a charge residue process. The other is a lower energy process, which would be expected for a process such as ion evaporation from the droplet surface within a cluster of solvent molecules.

Corresponding Author

*Corresponding Author E-mail: mvj@udel.edu

Present Addresses

†School of Information Science and Technology, University of Science and Technology of China, Hefei, Anhui 230026, China

Author Contributions

Experimental measurements and CFD modeling were performed by M.J.A. All authors contributed to the interpretation of results and writing of the manuscript. All authors have given approval to the final version of the manuscript.

Supporting Information

Supporting Information gives an extended description of the droplet evaporation model, plus seven additional figures mentioned in the text. Supporting_Information_Apsokardu_et_al (PDF)

Acknowledgment

The authors thank Dr. Federico G. Cruz of the University of Delaware for assistance with flame atomic absorption spectroscopy. This research was supported by the U. S. National Science Foundation under grant number CHE-1904765.

References

- (1) Iribarne, J. V; Thomson, B. A. On the Evaporation of Small Ions from Charged Droplets. *J. Chem. Phys.* **1976**, *64*, 2287–2294.
- (2) Dole, M.; Mack, L. L.; Hines, R. L.; Mobley, R. C.; Ferguson, L. D.; Alice, M. B.; Malcolm Dole, L. L. M.; Marck, L. L.; Hines, L.; Mobley, R. C.; et al. Molecular Beams of Macroions. *J. Chem. Phys.* **1968**, *49*, 2240–2249.
- (3) Konermann, L.; Ahadi, E.; Rodriguez, A. D.; Vahidi, S. Unraveling the Mechanism of Electrospray Ionization. *Anal. Chem.* **2013**, *85*, 2–9.
- (4) Kebarle, P.; Tang, L. From Ions in Solution To Ions in the Gas Phase. *Anal. Chem.* **1993**, 65, 972A-986A.
- (5) Znamenskiy, V.; Marginean, I.; Vertes, A. Solvated Ion Evaporation from Charged Water Nanodroplets. *J. Phys. Chem. A* **2003**, *107*, 7406–7412.
- (6) Konermann, L.; McAllister, R. G.; Metwally, H. Molecular Dynamics Simulations of the Electrospray Process: Formation of Nacl Clusters via the Charged Residue Mechanism. J. Phys. Chem. B 2014, 118, 12025–12033.
- (7) Larriba, C.; De La Mora, J. F.; Clemmer, D. E. Electrospray Ionization Mechanisms for Large Polyethylene Glycol Chains Studied through Tandem Ion Mobility Spectrometry. *J. Am. Soc. Mass Spectrom.* **2014**, 25, 1332–1345.
- (8) Consta, S.; In Oh, M.; Kwan, V.; Malevanets, A. Strengths and Weaknesses of Molecular Simulations of Electrosprayed Droplets. *J. Am. Soc. Mass Spectrom.* **2018**, 29, 2287–2296.

- (9) Duez, Q.; Metwally, H.; Konermann, L. Electrospray Ionization of Polypropylene Glycol: Rayleigh-Charged Droplets, Competing Pathways, and Charge State-Dependent Conformations. *Anal. Chem.* 2018, 90, 9912–9920.
- (10) Kebarle, P.; Verkerk, Udo, H. Electrospray: From Ions in Solution to Ions in the Gas Phase, What We Know Now. *Mass Spectrom. Rev.* **2009**, 28, 898–917.
- (11) Horan, A. J.; Apsokardu, M. J.; Johnston, M. V. Droplet Assisted Inlet Ionization for Online Analysis of Airborne Nanoparticles. *Anal. Chem.* **2017**, *89*, 1059–1062.
- (12) Apsokardu, M. J.; Kerecman, D. E.; Johnston, M. V. Ion Formation in Droplet-assisted Ionization. *Rapid Commun. Mass Spectrom.* **2018**, 1–7.
- (13) Peacock, P. M.; Zhang, W.-J.; Trimpin, S. Advances in Ionization for Mass Spectrometry. *Anal. Chem.* **2017**, *89*, 372–388.
- (14) Trimpin, S. Novel Ionization Processes for Use in Mass Spectrometry: 'Squeezing' Nonvolatile Analyte Ions from Crystals and Droplets. *Rapid Commun. Mass Spectrom*.
 2019, 33, 96–120.
- Trimpin, S.; Karki, S.; D. Marshall, D.; Inutan, E.; Meher, A.; Madarshahian, S.; A. Fenner,
 M.; Mcewen, C. Combining Novel and Traditional Ionization Methods for Mass
 Spectrometry for More Comprehensive Analyses. LC GC N. Am. 2018, 16, 12-17,27.
- (16) Hobbs, P. V; Cheng, R. J. Microdroplets and Water Drop Freezing. *Science*. **1971**, *173*, 849–850.
- (17) Cheng, R. J. Water Drop Freezing: Ejection of Microdroplets. Science. 1970, 170, 1395-

1396.

- (18) Wleklinski, M.; Li, Y.; Bag, S.; Sarkar, D.; Narayanan, R.; Pradeep, T.; Cooks, R. G. Zero Volt Paper Spray Ionization and Its Mechanism. *Anal. Chem.* **2015**, 87, 6786–6793.
- (19) Trimpin, S.; Wang, B.; Inutan, E. D.; Li, J.; Lietz, C. B.; Harron, A.; Pagnotti, V. S.; Sardelis, D.; McEwen, C. N. A Mechanism for Ionization of Nonvolatile Compounds in Mass Spectrometry: Considerations from MALDI and Inlet Ionization. *J. Am. Soc. Mass Spectrom.* 2012, 23, 1644–1660.
- (20) Özdemir, A.; Lin, J.-L.; Wang, Y. S.; Chen, C.-H. A Deeper Look into Sonic Spray Ionization. *RSC Adv.* **2014**, *4*, 61290–61297.
- (21) Teunissen, S. F.; Eberlin, M. N. Transferring Ions from Solution to the Gas Phase: The Two Basic Principles. *J. Am. Soc. Mass Spectrom.* **2017**, 28, 2255–2261.
- (22) Bernier, L.; Taesch, M.; Rauschenbach, S.; Reiss, J. Transfer Conditions and Transmission Bias in Capillaries of Vacuum Interfaces. *Int. J. Mass Spectrom.* **2020**, *447*.
- (23) Wagner, W.; Pruß, A. The IAPWS Formulation 1995 for the Thermodynamic Properties of Ordinary Water Substance for General and Scientific Use. *J. Phys. Chem. Ref. Data* **2002**, 31, 387–535.
- (24) Li, W.; Davis, E. J. Aerosol Evaporation in the Transition Regime. *Aerosol Sci. Technol*. **1996**, 25, 11–21.
- (25) Higashi, H.; Tokumi, T.; Hogan, C. J.; Suda, H.; Seto, T.; Otani, Y. Simultaneous Ion and Neutral Evaporation in Aqueous Nanodrops: Experiment, Theory, and Molecular Dynamics

- Simulations. Phys. Chem. Chem. Phys. 2015, 17, 15746–15755.
- (26) Zhifu, Z.; Guoxiang, W.; Bin, C.; Liejin, G.; Yueshe, W. Evaluation of Evaporation Models for Single Moving Droplet with a High Evaporation Rate. *Powder Technol.* **2013**, 240, 95–102.
- (27) Sula, C.; Grosshans, H.; Papalexandris, M. V. Assessment of Droplet Breakup Models for Spray Flow Simulations. *Flow, Turbul. Combust.* **2020**, No. 0123456789.
- (28) Zhao, F.; Yan, X.; Bo, H.; Meng, T.; Zeng, C.; Tan, S. Application of Droplet Motion and Phase Change Model in Containment Spray System. *Ann. Nucl. Energy* **2019**, *131*, 123–137.
- (29) Krzeczkowski, S. A. Measurement of Liquid Droplet Disintegration Mechanisms. *Int. J. Multiph. Flow* **1980**, *6*, 227–239.
- (30) Wierzba, A. Deformation and Breakup of Liquid Drops in a Gas Stream at Nearly Critical Weber Numbers. *Exp. Fluids* **1990**, *9*, 59–64.
- (31) Zilch, L. W.; Maze, J. T.; Smith, J. W.; Ewing, G. E.; Jarrold, M. F. Charge Separation in the Aerodynamic Breakup of Micrometer-Sized Water Droplets. *J. Phys. Chem. A* **2008**, *112*, 13352–13363.
- (32) Widmann, J. F.; Aardahl, C. L.; Davis, E. J. Observations of Non-Rayleigh Limit Explosions of Electrodynamically Levitated Microdroplets. *Aerosol Sci. Technol.* **1997**, 27, 636–648.
- (33) Niehaus, M.; Soltwisch, J. New Insights into Mechanisms of Material Ejection in MALDI

- Mass Spectrometry for a Wide Range of Spot Sizes. Sci. Rep. 2018, 8, 1–10.
- (34) Koubenakis, A.; Frankevich, V.; Zhang, J.; Zenobi, R. Time-Resolved Surface Temperature Measurement of MALDI Matrices under Pulsed UV Laser Irradiation. J. Phys. Chem. A 2004, 108, 2405–2410.
- (35) Maechling, C. R.; Clemett, S. J.; Engelke, F.; Zare, R. N. Evidence for Thermalization of Surface-Desorbed Molecules at Heating Rates of 108 K/S. *J. Chem. Phys.* **1996**, *104*, 8768–8776.
- (36) Rumble, J. R.; Lide, D. R.; Bruno, T. J. CRC Handbook of Chemistry and Physics [2019-2020]: A Ready-Reference Book of Chemical and Physical Data; 2019.
- (37) Aliyari, E.; Konermann, L. Formation of Gaseous Proteins via the Ion Evaporation Model (IEM) in Electrospray Mass Spectrometry. **2020**.
- (38) Wang, P.; Wesdemiotis, C.; Kapota, C.; Ohanessian, G. The Sodium Ion Affinities of Simple Di-, Tri-, and Tetrapeptides. *J. Am. Soc. Mass Spectrom.* **2007**, *18*, 541–552.
- (39) Amicangelo, J. C.; Armentrout, P. B. Relative and Absolute Bond Dissociation Energies of Sodium Cation-Alcohol Complexes Determined Using Competitive Collision-Induced Dissociation Experiments. *Int. J. Mass Spectrom.* **2011**, *301*, 45–54.
- (40) Rodgers, M. T.; Armentrout, P. B. Cationic Noncovalent Interactions: Energetics and Periodic Trends. *Chem. Rev.* **2016**, *116*, 5642–5687.
- (41) Loscertales, I. G.; Fernández De La Mora, J. Experiments on the Kinetics of Field Evaporation of Small Ions from Droplets. *J. Chem. Phys.* **1995**, *103*, 5041–5060.

- (42) Labowsky, M.; Fenn, J. B.; Fernandez De La Mora, J. A Continuum Model for Ion Evaporation from a Drop: Effect of Curvature and Charge on Ion Solvation Energy. *Anal. Chim. Acta* 2000, 406, 105–118.
- (43) Gamero-Castaño, M.; Fernandez De La Mora, J. Kinetics of Small Ion Evaporation from the Charge and Mass Distribution of Multiply Charged Clusters in Electrosprays. *J. Mass Spectrom.* **2000**, *35*, 790–803.
- (44) Hogan, C. J.; Fernández De La Mora, J. Tandem Ion Mobility-Mass Spectrometry (IMS-MS) Study of Ion Evaporation from Ionic Liquid-Acetonitrile Nanodrops. *Phys. Chem. Chem. Phys.* 2009, 11, 8079–8090.
- (45) Ahadi, E.; Konermann, L. Ejection of Solvated Ions from Electrosprayed Methanol/Water Nanodroplets Studied by Molecular Dynamics Simulations. *J. Am. Chem. Soc.* **2011**, *133*, 9354–9363.

Figures and Tables

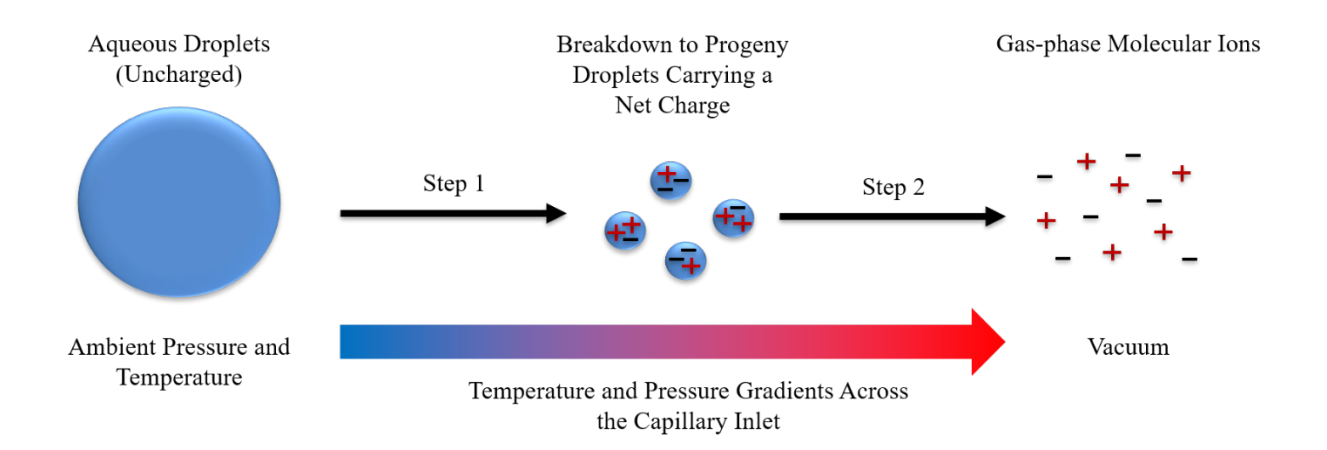


Figure 1. Schematic of the steps involved to form ions by droplet assisted ionization (DAI). Droplets undergo aerodynamic or thermal breakup, and ions are ejected into the gas phase from the charged progeny droplets.

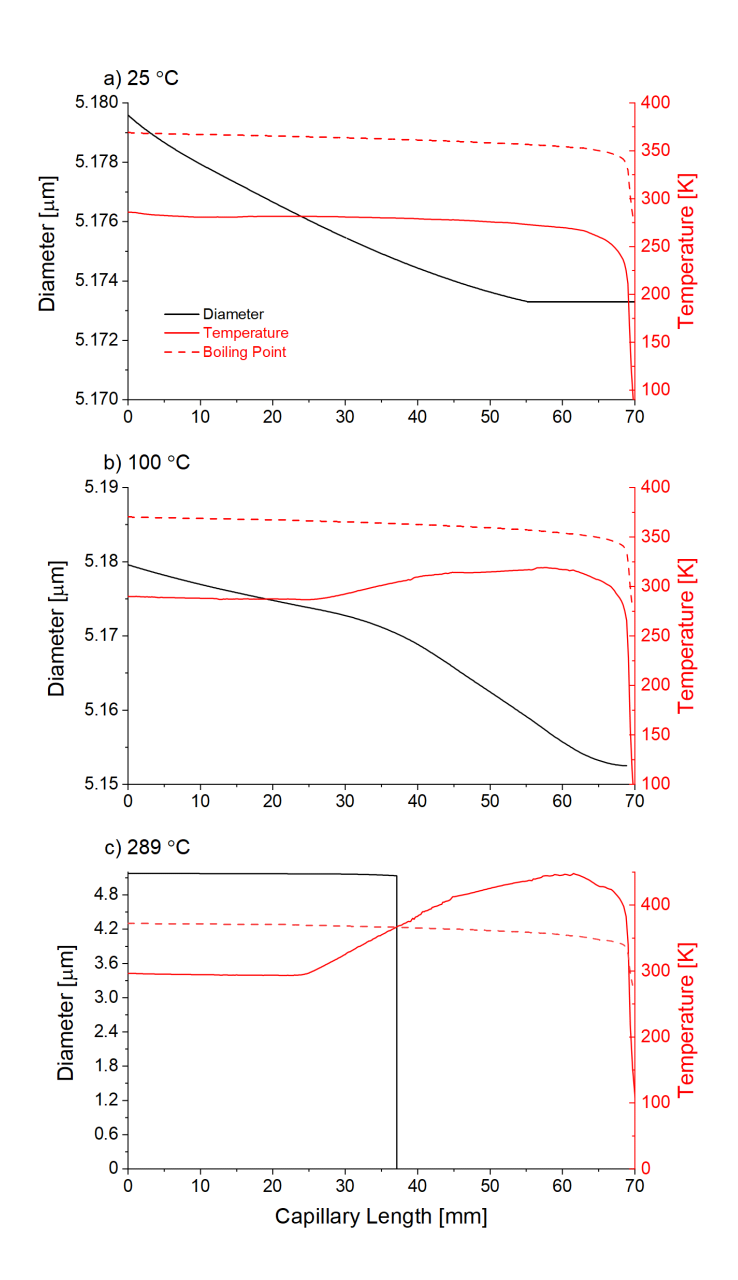


Figure 2. Evaporation of a 5.2 μ m dia. vs. distance through the capillary for a droplet moving along an air trajectory closest to the capillary wall, for wall temperatures of a) 25, b) 100, and c) 289 °C. The black line shows the droplet diameter. The red solid line shows the droplet temperature. The red dashed line shows the boiling point of water. Thermal breakup is indicated by flash evaporation of the droplet in c). Along the abscissa, the capillary entrance is 0 mm, the capillary exit is 69 mm, and the point at which heating begins is 20 mm.

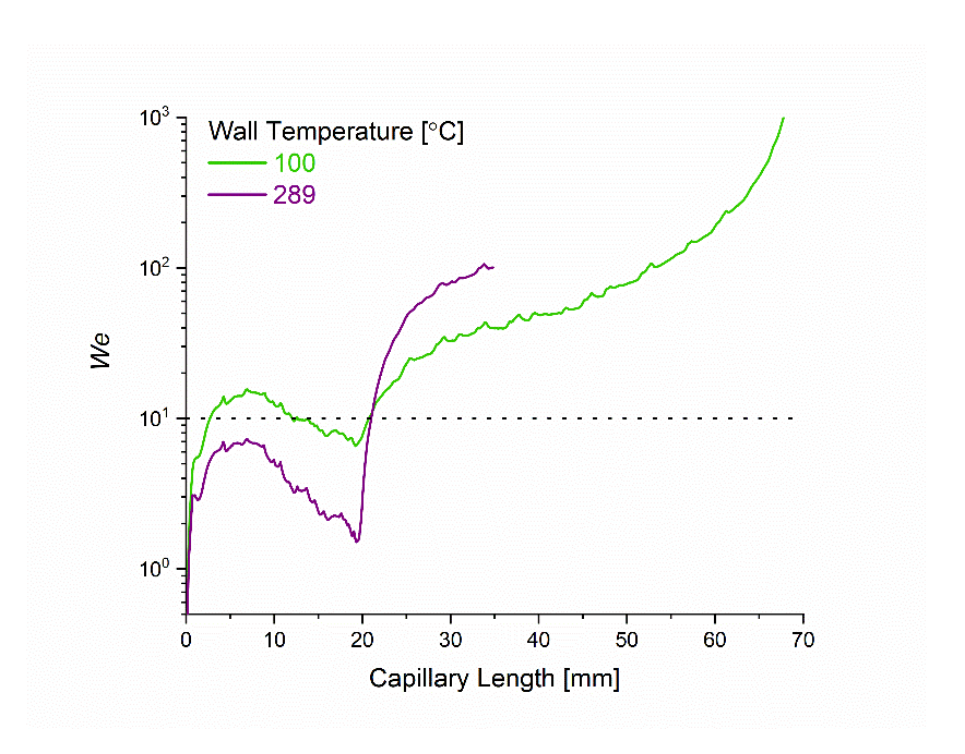


Figure 3. Weber number (We) of the 5.2 μ m dia. droplet in Figure 2 for wall temperatures of 100 (green) and 289 °C (purple). The dotted line shows We = 10, which is considered sufficient for aerodynamic breakup.

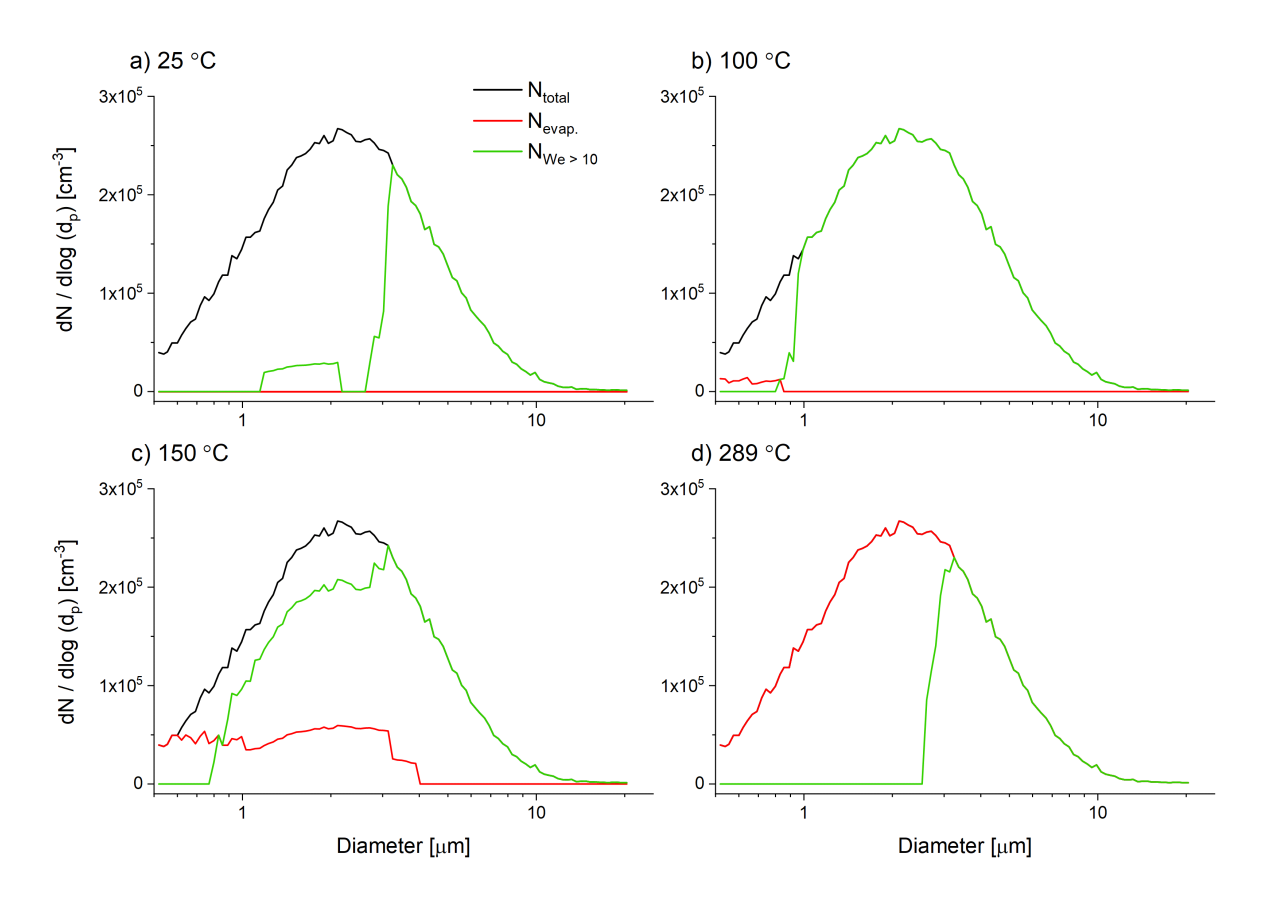


Figure 4. Number size-distribution of droplets (black) reconstructed from the dry particle size distribution measured for atomization of 100 μ M cortisone in water. Droplets capable of undergoing aerodynamic (green) and thermal (red) breakup are shown for capillary wall temperatures of a) 25, b) 100, c) 150, and d) 289 °C. In d), all droplets are capable of undergoing thermal breakup.

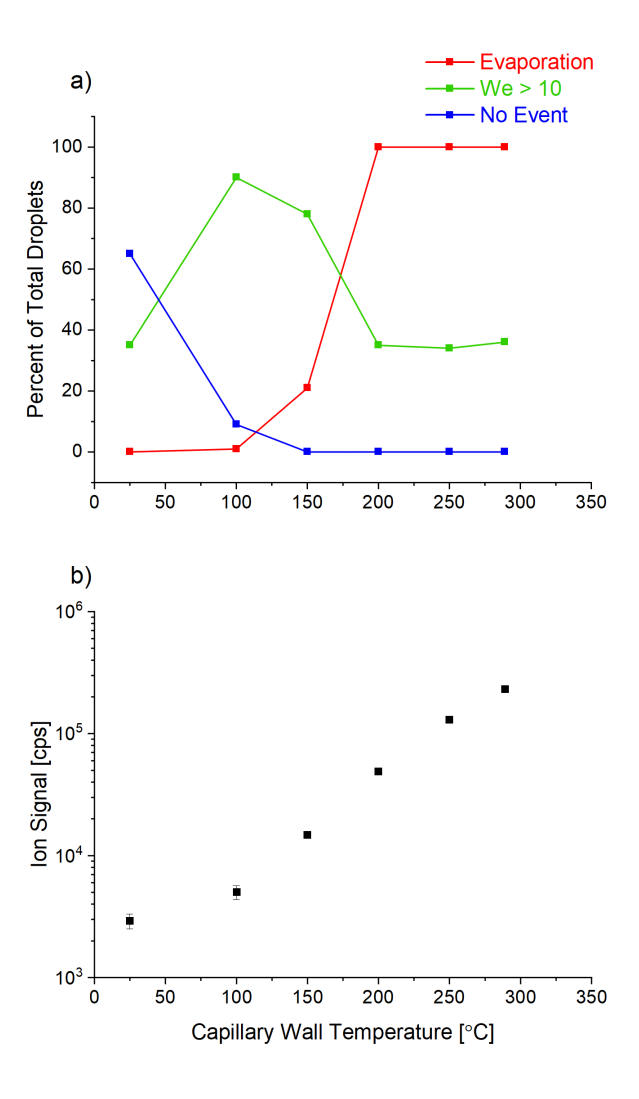


Figure 5. a) Percent of the droplets across the size distribution that are capable of aerodynamic (green) and thermal (red) breakup at each capillary wall temperature. 'No event' (blue) is defined as droplets that can undergo neither aerodynamic nor thermal breakup. At 25 °C, many 'no event' droplets freeze and may undergo shattering to produce ions. (b) Experimentally measured ion signal as counts per second (cps) at each wall temperature for droplets generated from $100 \mu M$ cortisone in water.

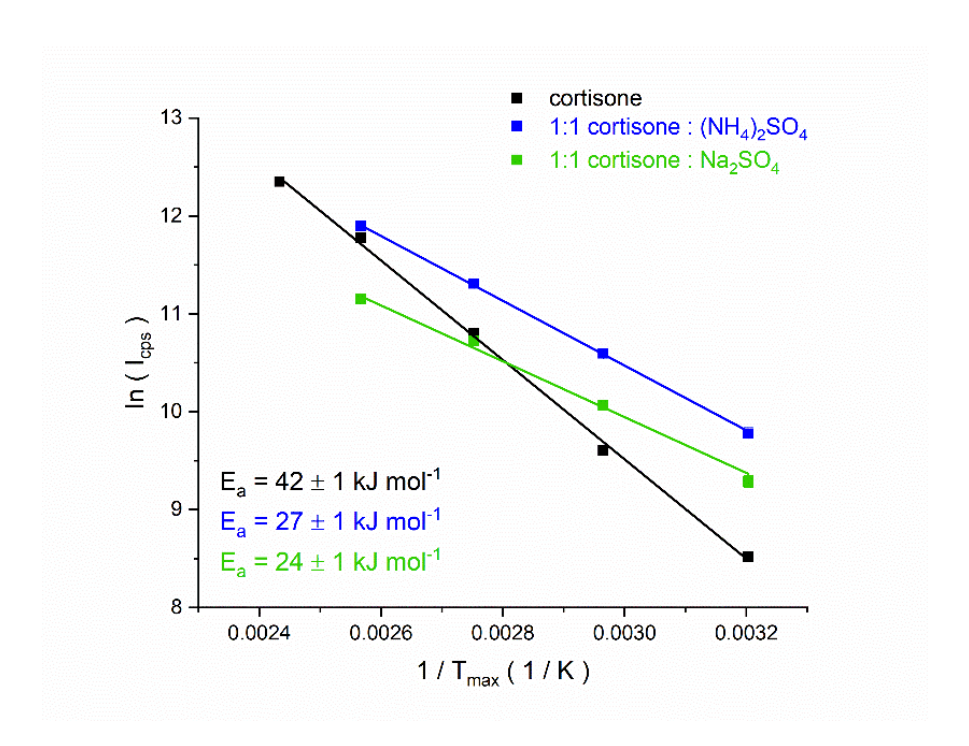


Figure 6. Arrhenius plot for droplets generated from aqueous solutions containing 100 μM cortisone. Black is cortisone alone. Blue is a 1:1 mole ratio of cortisone and (NH₄)₂SO₄. Green is a 1:1 mole ratio of cortisone and Na₂SO₄. Error bars represent one standard deviation of the signal intensity, and uncertainty in the activation energy is determined from the standard error of the slope of the line.

Table 1. Activation energies (E_a) for ion formation from droplets containing nonionic solutes (left) and salts (right).

Nonionic Solutes	E _a (kJ mol ⁻¹)	Salts	E _a (kJ mol ⁻¹)
sucrose	39 ± 3	1:1 cortisone : cesium iodide	24 ± 2
cortisone	42 ± 1	1:1 cortisone : ammonium sulfate	27 ± 1
polypropylene glycol (PPG)	41 ± 3	1:1 cortisone : sodium sulfate	24 ± 1
		cesium iodide	22 ± 5
		tetrabutylammonium chloride	19 ± 2

The polypropylene glycol concentration is $10 \,\mu\text{M}$. All other concentrations are $100 \,\mu\text{M}$.

TOC Figure

